The Astronomical Journal, 159:206 (6pp), 2020 May https://doi.org/10.3847/1538-3881/ab7fae

Mars Upper Atmospheric Temperature and Atomic Oxygen Density Derived from the O I 130.4 nm Emission Observed by NASA's MAVEN Mission

Jianqi Qin
School of Earth and Space Sciences, Peking University, Beijing, People's Republic of China; jqqin@pku.edu.cn
Received 2020 January 3; revised 2020 March 11; accepted 2020 March 11; published 2020 April 13

Abstract

The abundance of atomic oxygen is a major unknown for the Mars upper atmosphere, and systematic measurements of this key species is a primary objective of NASA's Mars Atmosphere and Volatile Evolution (MAVEN) mission. Moreover, the Martian dayside temperature structure and its variability has been a subject of considerable debate in the past. In this study, an inversion analysis of the periapsis limb scans of the O I 130.4 nm emission observed by MAVEN is performed to quantify the neutral temperature and atomic oxygen abundance in the Mars upper atmosphere. Our analysis yields unprecedented resolution of the spatial variation of Mars atomic oxygen, showing that its exobase density decreases with the solar zenith angle (SZA) from ~0° to 60° by about an order of magnitude, from $\sim 10^8$ to $\sim 10^7$ cm^{-3} near perihelion (2015 April) and from $\sim 10^7$ to $\sim 10^6$ cm^{-3} near aphelion (2017 November). For a given SZA the exobase densities near perihelion are about an order of magnitude higher than those near aphelion. The [O]/[CO_2] mixing ratio at 130 km altitude can vary from ~0.1% to 4.6%, which also decreases with increasing SZA. Moreover, it is shown that the Mars exobase temperature does not vary significantly with SZA from ~0° to ~60°, which is estimated to be ~239.2 ± 27.6 K near perihelion and ~162.4 ± 19.9 K near aphelion, with a difference of 76.8 K between these two seasonal extremes.

Unified Astronomy Thesaurus concepts: Mars (1007); Atmospheric composition (2120); Aeronomy (22)

1. Introduction

Atomic oxygen, O, is a key atmospheric constituent that overtakes carbon dioxide, CO_2, above ~200 km altitude to be the dominant neutral species in the Mars upper thermosphere and lower exosphere. The distribution of this major species has critical impacts on the thermal structure, composition, chemistry, and dynamics of the Mars atmosphere and ionosphere, as well as on the escape of gas into space that was an important or possibly even the dominant process in driving the planet's climate change over time (e.g., Bougher et al. 2015a; Medvedev et al. 2016). Owing to the critical role of atomic oxygen in governing the state of the atmosphere of Mars, quantification of its abundance is of essential importance for achieving the science objectives of NASA's Mars Atmosphere and Volatile Evolution (MAVEN) mission, which was launched in 2013 to study the composition and structure of the atmosphere and ionosphere of Mars, to estimate the current and historical atmospheric escape rates, and to determine the importance of loss to space in changing the Mars climate and habitability through time (Jakosky et al. 2015a, 2015b).

MAVEN characterizes the spatial and temporal variabilities of Mars' atmosphere and ionosphere through both in situ and remote measurements of the state variables. Specifically, the Neutral Gas and Ion Mass Spectrometer (NGIMS) measures the in situ densities of neutral and ionic species, e.g., CO_2, O, and O_2^+, along the spacecraft track over the 125–500 km altitude region (Mahaffy et al. 2015), while the Imaging UltraViolet Spectrograph (IUVS) derives neutral densities from remote sensing of the Mars atmospheric ultraviolet (UV) emissions (McClintock et al. 2015). In the literature, the upper atmospheric O densities were obtained either from the NGIMS in situ measurements (Mahaffy et al. 2015) or from inversion of the IUVS coronal scans of the O I 130.4 nm emission (Chaufray et al. 2015). The upper atmospheric temperature profiles were derived from the scale heights of neutral species such as Ar and CO_2 measured by NGIMS (Bougher et al. 2017; Stone et al. 2018) or from the scale heights estimated using the middle ultraviolet emissions such as the CO Cameron bands and the CO_2^+ ultraviolet doublet observed by IUVS (Evans et al. 2015; Jain et al. 2015).

Those different types of measurements have significantly advanced the study of the upper atmospheric state of Mars and its variability. However, owing to the limited spatial and temporal coverages of those measurements, our understanding of the global and seasonal variabilities of the upper atmosphere of Mars is still far from complete. Recently, Ritter et al. (2019) presented an overview of the periapsis limb scans of the O I 130.4 nm emissions observed by MAVEN over two Martian years (32–33), showing the potential of this data set to be useful for quantifying the Mars upper atmospheric variability. In this work, we present an inversion analysis of those periapses limb scans using a radiative transfer model that has been developed recently by Qin & Harding (2020) assuming angle-dependent partial frequency redistribution (Meier & Lee 1978, Meier 1981). The derived Mars upper atmospheric temperature and O density are compared with those documented in the literature. We demonstrate consistency of our inversion results with previous measurements, and show clear seasonal variation and unprecedented spatial resolution of the derived state variables.

2. Observations and Model

The MAVEN spacecraft arrived at Mars on 2014 September 21 and went into an elliptical orbit with a period of 4.5 hr, periapsis altitude of ~150 km (with several campaigns down to ~125 km), apoapsis of ~6200 km, and an inclination of 74° (Jakosky et al. 2015a). The IUVS instrument aboard MAVEN uses a long, narrow slit (11° × 0°.06) in the telescope focal plane to provide entrance to the spectrograph and define the instrument field of view (McClintock et al. 2015). At an instant

in time, the instrument uses array detectors to record images that contain spectra in one dimension (with a spectral resolution of ∼0.6 nm) and spatial variations along the slit in the other dimension. Altitude profiles are built up by successively displacing the slit perpendicular to its long axis and recording additional spectral–spatial images. The observations are organized by orbit phase: periapsis, apoapsis, and "orbit sides." During the periapsis phase, IUVS scans the limb over the altitude range from ∼100 to ∼250 km with a spatial resolution of ∼5 km. Twelve individual scans of the O I 130.4 nm emission are made in the 23 minute segment when the spacecraft altitude is less than ∼500 km, and 21 measurements are made during each scan. The slit image at the detector is divided into seven spatial bins along the slit, which are associated with slightly different tangent altitudes. During the other two phases, the O I 130.4 nm emission is observed either over the Martian disk with ∼120 km horizontal spatial resolution or from the disk to the exosphere with a vertical resolution of tens of kilometers (McClintock et al. 2015). Among these three observation types, the periapsis limb scans have the highest spatial resolution, providing an excellent data set for the analysis of the Mars upper atmospheric temperature and O density, which is the primary objective of this study.

To derive the temperature and O density, transport of the O I 130.4 nm resonance emission in the optically thick Martian atmosphere must be properly simulated. For this purpose we use a Monte Carlo radiative transfer (MCRT) model that has been recently developed by Qin & Harding (2020) for the study of geocoronal O I 130.4 nm emission. The MCRT model is based on the algorithm of Meier (1982) and uses an angle-dependent partial frequency redistribution function (Hummer 1962, Equation (2.22.2)). Qin & Harding (2020) have validated their MCRT model by comparing with three other radiative transfer models, which were developed based on distinctly different numerical techniques by Qin et al. (2015), Meier (1982), and Gladstone (1982), respectively. For the purpose of this study the MCRT model is adapted for the simulation of Mars coronal O I 130.4 nm emission. For each line of the triplet, the resonant absorption cross-section is calculated using the parameters given by Meier (1991, Table 4), and the CO_2 pure absorption cross-section is obtained from the measurements of Starr (1976). For the sources of excitation, we consider only the resonant scattering of the solar photons and neglect the photoelectron impact excitation, since the latter has been estimated to contribute only a few percentages to the total brightness (e.g., Strickland et al. 1973; Chaufray et al. 2009, 2015). The solar flux at 130.4 nm is taken from the MAVEN Extreme Ultraviolet Monitor (EUVM; Eparvier et al. 2015), and the solar spectral shape is taken from the work of Gladstone (1992).

In the MCRT model, the O and CO_2 density profiles as well as the neutral temperature need to be specified for the calculation of photon transport in the Mars coronal region. Following the approach of Chaufray et al. (2015), the one-dimensional O density profile is divided into two parts: a thermospheric profile from 80 km to the exobase and an exospheric profile from 200 to 1000 km. Below the exobase, the O and CO_2 density profiles are calculated by solving the coupled diffusion and hydrostatic equations (Hunten 1973), with the temperature as a function of altitude given by Krasnopolsky (2002),

$$T(h) = T_\infty - (T_\infty - 125)\exp\left(-\frac{(h - h_0)^2}{\alpha T_\infty}\right), \quad (1)$$

where T_∞ is the exobase temperature, $h_0 = 90$ km, and $\alpha = 11.4$ according to the relationship approximated by Krasnopolsky (2002). The CO_2 density at 80 km is chosen to be 2.6×10^{13} cm^{-3} (Krasnopolsky 2002). Above the exobase, the Chamberlain model is used to describe the exospheric O density (Chamberlain 1963). In this way, the simulated O density from 80 to 1000 km can be fully determined using only two salient parameters: the exobase temperature and density (Chaufray et al. 2015). An inverse process is performed to find the two parameters that lead to the best fits of the simulated and the observed radiances. During the inversion process, the MCRT model is used as the forward model to simulate the radiance profiles for given temperature and density profiles. The optimal parameters leading to the best fits are obtained through a least-squares fitting process. It should be noted that the MCRT model is not deterministic, which introduces an uncertainty in the inversion. To minimize this effect, we use a sufficiently large number of testing particles in the MCRT model to ensure that with different initial guesses the inversion converges to similar results. We then select the best fit from those multiple fits that are obtained using different initial guesses to derive the temperature and O density.

3. Results

We select the periapsis limb scans associated with orbits 979, 981, 982, 984, 985, and 1051 observed during 2015 April (near perihelion with the Sun–Mars distance ≃1.46 au and the solar longitude Ls ≃319°–326°) and orbits 5999, 6000, 6002, 6030, 6031, and 6032 observed during 2017 November (near aphelion with the Sun–Mars distance ≃1.66 au and the Ls ≃82°–85°) from the MAVEN IUVS L1B v13 data products for this analysis. We make selections from these two distinctly different time periods in order to investigate the impact of the Sun–Mars distance on the Mars upper atmospheric state. The specific orbits are selected based on two criteria: (1) the 12 periapsis limb scans associated with each orbit are recorded over a large range of solar zenith angles (SZA) from ∼0° to ∼60°. The purpose is to investigate the variations of temperature and O density with SZA. (2) Similar to the approach used by Chaufray et al. (2015) in their analysis of coronal scans, we compute the observed radiances by spectral integration assuming a residual linear background from the IUVS L1B data. To minimize bias that might be introduced by the background subtraction process, we select those orbits that exhibit only a small background emission in their periapsis limb scans.

Figure 1 shows the periapsis limb scans associated with orbits 1051 and 6002. In panel (a) the lines represent the radiance profiles associated with the 12 scans observed along orbit 1051. Note that each scan is actually an image, which has 21 pixels in the vertical direction (i.e., 21 measurements were made during each scan to sample different altitudes) and seven pixels in the horizontal direction (i.e., seven bins along slit). For clarity only the radiance profile associated with the central bins are plotted in panel (a). The line colors are used to distinguish the SZAs at which the corresponding scans are

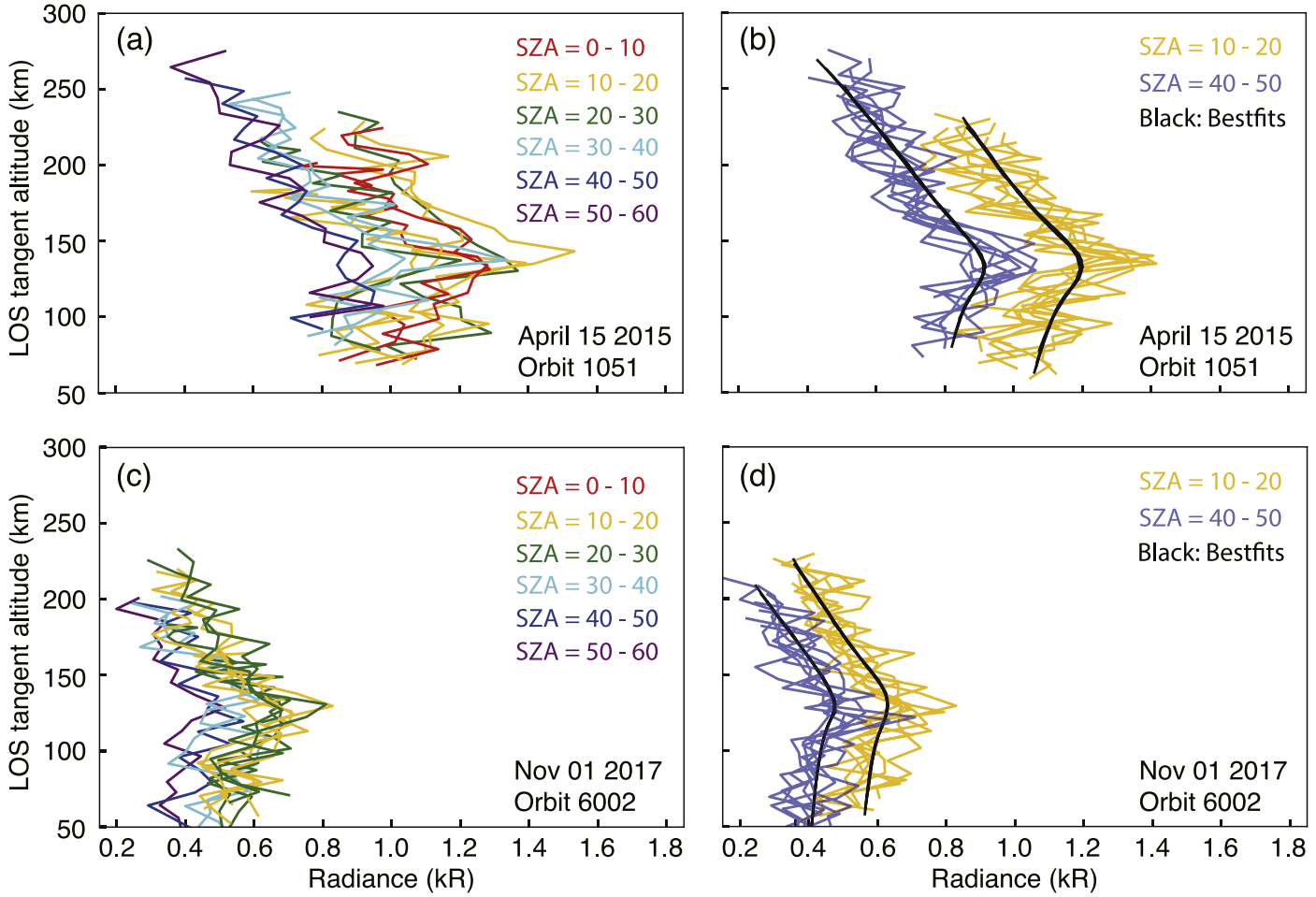

Figure 1. (a) Twelve periapsis limb scans of the O I 130.4 nm emission observed during orbit 1051. For each scan only the radiance profile associated with the central one of the seven bins along the slit is shown. The colors represent different SZAs at which the corresponding scans are observed. (b) Colored: all seven radiance profiles of two representative scans associated with orbit 1051. Black: the best-fit radiance profiles obtained from the inversions. (c, d): the same as (a, b) but for orbit 6002.

observed. Similarly, panel (c) shows the scans observed along orbit 6002. It can be seen that the radiances observed at small SZAs are generally larger than those observed at large SZAs. Moreover, the radiances observed along orbit 1051 are about a factor of ∼2–3 larger than those along orbit 6002. By examining the MAVEN EUVM level 3 v11 data products, we find that the solar 130.4 nm flux (i.e., the solar flux between 130 and 131 nm reconstructed from the EUVM measurements at 0–7 nm, 17–22 nm, and 121.6 nm; Eparvier et al. 2015) is 5.02×10^9 photons cm^{-3} s^{-1} during orbit 1051, which is only a factor of 1.33 higher than that of 3.78×10^9 photons cm^{-3} s^{-1} during orbit 6002. The considerable difference between the two factors implies that the upper atmospheric O density during orbit 1051 should be higher than that of orbit 6002, which will be demonstrated later using the inversion results.

Figure 1(b) shows all seven radiance profiles of two representative scans associated with orbit 1051, and Figure 1(d) shows two examples associated with orbit 6002. The four scans are observed either at 10°–20° SZA or at 40°–50° SZA. Many of such individual scans are inverted in this study to derive Mars upper atmospheric temperature and O density. In the inversion of the each individual scans, we use the MCRT model to generate seven radiance profiles during each iteration for comparison with the observations. The black lines in Figure 1(b), (d) represent the best-fit radiance profiles generated using the MCRT model, which agree well with the observations. The temperature and O density profiles leading to those best fits are considered as the derived temperature and density. Note that we select the orbit 1051 for illustration in Figure 1 (as well as in Figure 2) because this orbit includes small SZA $\lesssim 12°$ (down to ∼3°), which are not included in other orbits (979–985). Moreover, the intensities observed during this orbit are higher than the others, leading to a larger signal-to-noise ratio.

Figure 2 shows the exobase temperature, exobase O density, and the $[O]/[CO_2]$ mixing ratio at 130 km altitude derived by inverting the periapsis limb scans associated with orbits 1051 and 6002. As indicated in Section 2, the exobase temperature and exobase O density fully determine the O density profile from 80 to 1000 km altitude. The $[O]/[CO_2]$ mixing ratio is an important element in the global heat budget of the Mars thermosphere (Chaufray et al. 2009), which can also be estimated in our inversions since the CO_2 density profile is calculated by solving the coupled diffusion and hydrostatic equations (Hunten 1973). In Figure 2, the numbers "1," "2," and "12" are used to indicate the time sequence of the scans, with "1" being the earliest and "12" being the latest. The purpose of this labeling is to show how the derived exobase temperature and O density vary with the spacecraft location along the orbits. The color of the markers indicates the latitude

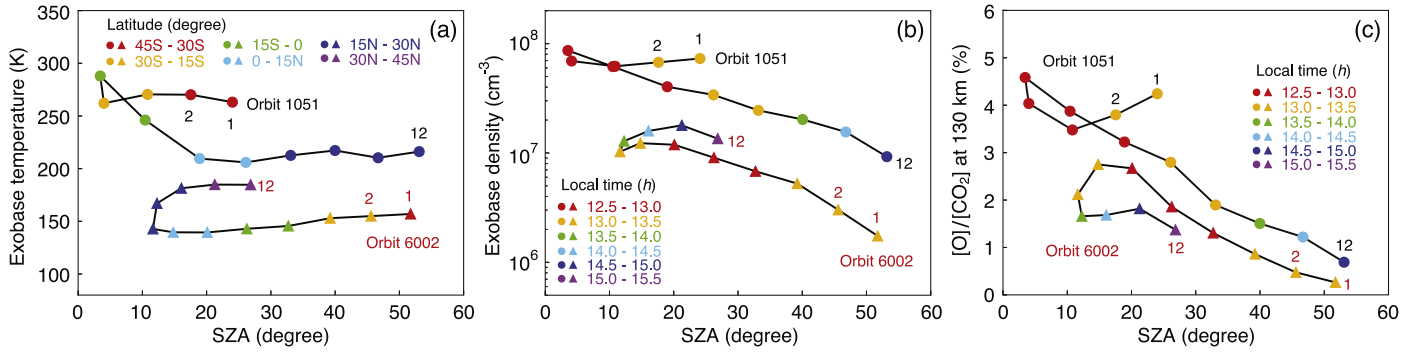

Figure 2. (a) Exobase temperature derived from the periapsis limb scans associated with (dots) orbit 1051 and (triangles) orbit 6002. The numbers "1" and "2" indicate the inbound side of the orbit while "12" indicates the outbound side. The color of the markers indicates the tangent point latitude of the eleventh LOS (i.e., the middle one of the 21 LOSs) for each scan. (b–c) The derived exobase O density and the [O]/[CO_2] mixing ratio at 130 km altitude. The color of the markers indicates the local time at the tangent point of the eleventh LOS for each scan.

and local time at the tangent point of the eleventh line of sight (LOS), which are almost identical to the mean latitude and local time at the tangent points of the 21 LOSs for each scan. For orbit 1051, the local time varies from ∼12.6 to ∼14.8 hr (0 = midnight, 12 = noon), and the latitude varies from about −41.°8 to 29.°9 (i.e., MAVEN is moving from the southern to northern hemisphere). For orbit 6002, the local time varies from 12.8 to 15.2 hr, and the latitude varies from −31.°9 to 36.°4.

As shown in Figure 2(a), the exobase temperature does not vary significantly with SZA along the inbound or outbound portions of orbit 1051. However, there is a ∼40 K difference between the exobase temperature derived from the inbound and the outbound sides. The exobase temperature along orbit 6002 also exhibits a similar difference. Figure 2(b) shows that the exobase density deceases with SZA by about an order of magnitude from ∼0° to 60°, which also tends to decrease with local time from ∼12.5 to 15.5 hr. Figure 2(c) shows that the [O]/[CO_2] mixing ratio at 130 km altitude varies with SZA as well as with local time. We note that it cannot be determined whether the temperature difference shown in Figure 2(a) is physical or is simply due to the uncertainties of the inversion. It can neither be determined whether it is a common feature because the periapsis limb scans with SZA < 60° are usually observed along only the inbound side or the outbound side of the orbits. One possibility is that the difference is due to latitudinal variation of the temperature, since the spacecraft moved over a large latitude range of ∼70° from the southern to northern hemisphere when those limb scans were observed. However, it is also possible that the difference is (partially) due to the uncertainties of the inversion. As indicated in Equation (1), the temperature as a function of altitude is approximated using the relationship from Krasnopolsky (2002). In our inversion, only the exobase temperature T_∞ is variable in the temperature profile. The other parameters, h_0 and α, are fixed using the values of 90 km and 11.4 given by Krasnopolsky (2002). Additional inversions show that if h_0 can vary from 85 to 95 km and/or that α can vary from 7.4 to 15.4, the derived exobase temperature can have a difference of up to ∼20 K from those shown in Figure 2.

Since the derived temperature associated with individual orbits may exhibit large uncertainties, we analyze a number of orbits in order to obtain a statistical comparison between the two seasonal extremes. Figure 3 shows the exobase temperature, exobase O density, and the [O]/[CO_2] mixing ratio at 130 km altitude derived from the periapsis limb scans associated with all 12 orbits selected for this analysis, including the six orbits during 2015 April and the other six during 2017 November. It can be seen that the exobase temperature, the exobase O density, and the [O]/[CO_2] mixing ratio at 130 km altitude derived from the limb scans observed near perihelion are higher than those near aphelion, which indicates that the Sun–Mars distance has a significant impact on the Mars upper atmospheric state. Using all the derived temperature values shown in Figure 3(a), we calculate that near perihelion the mean exobase temperature is 239.2 K with a standard deviation of 27.6 K, and that near aphelion the mean is 162.4 K with a standard deviation of 19.9 K. The mean temperature associated with the two time periods has a 76.8 K difference. Figure 3(b) shows that the exobase O density varies from ∼10^6 to ∼10^8 cm^{-3} for SZA < 60°. Moreover, the exobase density decreases with SZA by about an order of magnitude from ∼0° to 60°, and for a given SZA the density values near perihelion are about an order of magnitude higher than those near aphelion. Figure 3(c) shows that the [O]/[CO_2] mixing ratio at 130 km altitude can vary from ∼0.1% to 4.6%, which is also dependent on SZA and the Sun–Mars distance.

As noted by Chaufray et al. (2015), the exobase temperature and density derived from the O I 130.4 nm emission observed by MAVEN are sensitive to the IUVS instrument calibration, which has an uncertainty of ∼25%. To investigate the effect of this uncertainty, we scale the observed intensities by a factor of 0.75 or 1.25, and repeat all the inversions presented in Figure 3. We first compare the mean exobase temperatures. With a scaling factor of 0.75 (1.25), the exobase temperature is estimated to be 233.9 ± 33.3 K (251.9 ± 40.7 K) near perihelion and 165.9 ± 21.6 K (161.9 ± 18.2 K) near aphelion. The differences of these mean temperatures relative to those estimated without scaling are less than ∼12 K. We further compare the mean ratios between the exobase densities estimated with and without scaling. With a scaling factor of 0.75 (1.25), the mean ratio is 0.31 ± 0.07 (1.96 ± 0.18) near perihelion and 0.32 ± 0.04 (1.74 ± 0.15) near aphelion. These density ratios agree well with the results of Chaufray et al. (2015), indicating that the estimations are indeed sensitive to the IUVS instrument calibration.

4. Discussion

Prior to the MAVEN mission, the abundance of O atoms is a major unknown for the Mars upper atmosphere, with only a few constraints documented in the literature, e.g., from the

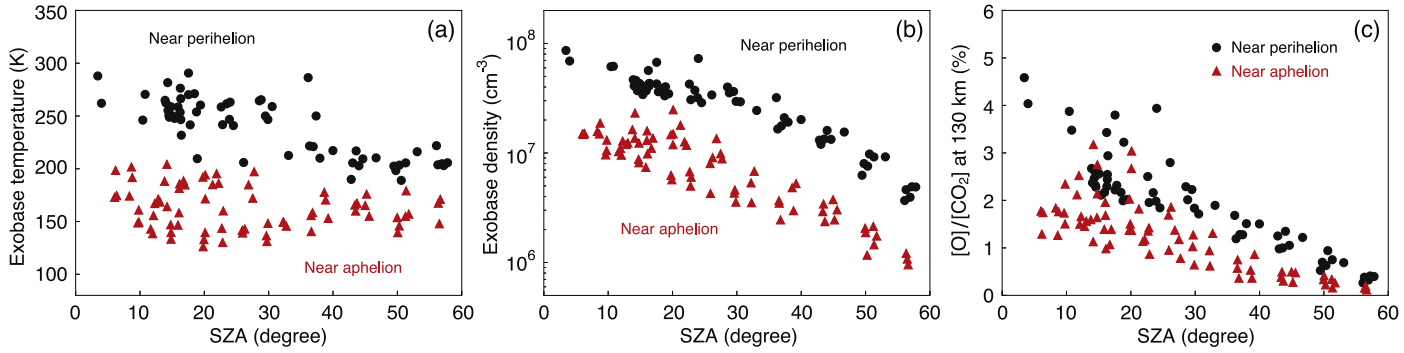

Figure 3. (a) The exobase temperature, (b) the exobase O densities, and (c) the $[O]/[CO_2]$ mixing ratio at 130 km altitude derived from the MAVEN IUVS periapsis limb scans associated with (black dots) orbits 979, 981, 982, 984, 985, and 1051 and (red triangles) orbits 5999, 6000, 6002, 6030, 6031, and 6032.

measurements of the Viking landers (Hanson et al. 1977; Nier & McElroy 1977), the Mariner missions (Strickland et al. 1972; Stewart et al. 1992), and the Mars Express mission (Chaufray et al. 2009). Particularly, by analyzing several observations of the O I 130.4 nm emission from Mars Express, Chaufray et al. (2009) found that the O density at the exobase is about 1.2×10^7 cm^{-3} for SZAs between 20° and 55° and decreases by a factor of 2 for SZAs between 55° and 90°. The $[O]/[CO_2]$ mixing ratio was estimated in a few cases to be 0.5%–1.0% at 135 km by Strickland et al. (1972), 1.25% at 130 km by Hanson et al. (1977), and 0.6%–1.2% at 135 km by Chaufray et al. (2009). With the MAVEN mission, systematic measurements of this key species (both spatially and temporally) become possible, which are needed to constrain the heat budget and chemistry of the dayside thermosphere (Bougher et al. 2015a) as well as to quantify the escape of gas into space (Deighan et al. 2015; Leblanc et al. 2017). To date, the O I 130.4 nm emission observed by MAVEN IUVS has been analyzed in two studies to investigate the cold population of atomic oxygen in the Mars upper atmosphere (Chaufray et al. 2015; Ritter et al. 2019). Chaufray et al. (2015) presented an inversion analysis of the IUVS coronal scans of the O I 130.4 nm emission and showed that the derived exobase O density near perihelion is 7.7, 4.1, 3.7, and 1.7×10^7 cm^{-3} for orbits 236, 349, 460, and 570, respectively. More recently, Ritter et al. (2019) presented an overview of the periapsis limb scans of O I 130.4 and 135.6 nm emissions observed by MAVEN IUVS over two Martian years (32–33). In their work, clear variations of the maximum emission brightness and altitude with season, SZA, and latitude have been shown, which reflect a strong variability of the Martian atmosphere. Those authors also performed a forward modeling study to investigate the sensitivity of those two emissions to the atmospheric constituents (O and CO_2), the temperature profile, and the solar flux, in which the $[O]/[CO_2]$ mixing ratio was derived to be 3.1% and 3.0% at 130 km for two data sets collected at Ls = 350° in Martian year 32 and 33.

In the present study, an inversion analysis of the IUVS periapsis limb scans of the O I 130.4 nm emission has been performed, which shows that the exobase O density near perihelion can vary from $\sim 5 \times 10^6$ to 10^8 cm^{-3} depending on the SZA. These density values are in good agreement with the results of Chaufray et al. (2015). Our analysis also demonstrates that the exobase density decreases with SZA, which is consistent with the NGIMS density measurements analyzed by Mahaffy et al. (2015) and the inversion results of Chaufray et al. (2009). Moreover, the exobase density tends to decrease with local time from ~12.5 to 15.5 hr (see Figure 2(b)), which is consistent with the simulation results of the Mars Global Ionosphere-Thermosphere Model (Bougher et al. 2015b, Figures 2 and 3). Such a tendency can be clearly seen for orbit 1051, but is less evident for orbit 6002, which is likely because for the aphelion condition the exobase density also varies significantly with latitude (Bougher et al. 2015b, Figure 3). In addition, our inversion results show that the $[O]/[CO_2]$ mixing ratio at 130 km altitude can vary from ~0.1% to 4.6%, which agrees with the large variability of the mixing ratios reported in the literature (Strickland et al. 1972; Hanson et al. 1977; Chaufray et al. 2009; Ritter et al. 2019). Noted that MAVEN IUVS records only one coronal scan during each orbit, more specifically, during the outbound phase of each orbit a coronal scan is observed from the disk to the exosphere with a spatial resolution of tens of kilometers. Each coronal scan is associated with a relatively small range of SZA, namely, the SZA at the LOS tangent point does not vary significantly during one coronal scan. In comparison, IUVS records 12 periapsis limb scans when MAVEN is passing through the thermosphere, with each scan having a much higher spatial resolution of ~5 km. This enables more accurate quantification of the thermospheric O density and temperature. Moreover, each of the 12 periapsis limb scans are observed at different SZAs, and together they can be used to derive the variation of the O density with a high spatial resolution, as demonstrated in this study.

As noted by Bougher et al. (2017), there was considerable debate regarding the Martian dayside temperature structure and its variability since the first Mariner ultraviolet spectrometer measurements were made in the early 1970s. Pre-MAVEN in situ and remote measurements show that the solar cycle and seasonal variations of the Martian dayside exospheric temperatures could be from ~150 to ~400 K, which are most uncertain for solar moderate-to-maximum conditions due to little available data (Bougher et al. 2017). By deriving the temperature from the CO_2 density scale heights using the MAVEN NGIMS measurements, Bougher et al. (2017) found that the temperature decreased after perihelion from 242.0 ± 15.5 K to 174.7 ± 24.2 K at aphelion, a difference of ~70 K between these two seasonal extremes. In our analysis using the IUVS periapsis limb scans of the O I 130.4 nm emission, we find 239.2 ± 27.6 K near perihelion and 162.4 ± 19.9 K near aphelion, with a difference of 76.8 K. Given that the NGIMS measurements analyzed by Bougher et al. (2017) and the IUVS measurement analyzed in the present study are obtained at different times, we consider that

the temperature variability derived using these two fundamentally different approaches agrees very well with each other. Together these different types of measurements can provide useful information to advance our understanding of the Martian dayside temperature structure.

5. Conclusions

In this study, the periapsis limb scans of the O I 130.4 nm emission observed by the IUVS instrument aboard NASA's MAVEN mission are analyzed using a radiative transfer model to quantify the temporal and spatial variations of the Mars upper atmospheric temperature and O density. Our inversion results show that the Mars exobase temperature does not vary significantly with SZA from $\sim 0^\circ$ to $\sim 60^\circ$. In this SZA range the mean exobase temperature is 239.2 ± 27.6 K near perihelion (2015 April) and 162.4 ± 19.9 K near aphelion (2017 November), with a difference of 76.8 K between these two seasonal extremes. Our inversion results also show that the exobase O density can vary from $\sim 10^6$ to $\sim 10^8\,\mathrm{cm}^{-3}$ for SZA $< 60^\circ$. The derived exobase O density decreases with SZA by about an order of magnitude from $\sim 0^\circ$ to 60°, and for a given SZA the density values near perihelion are about an order of magnitude higher than those near aphelion. The $[O]/[CO_2]$ mixing ratio at 130 km altitude can vary from $\sim 0.1\%$ to 4.6%, which also decreases with increasing SZA. Our results demonstrate that inversion of the O I 130.4 nm periapsis limb scans is a powerful means for quantifying the seasonal and global variations of Mars upper atmospheric state with a high spatial resolution, which is one of the primary objectives of the MAVEN mission.

The MAVEN IUVS L1B v13 data products and the EUVM level 3 data products are archived in NASA's Planetary Data System (https://atmos.nmsu.edu/data_and_services/atmospheres_data/MAVEN/maven_main.html). The IUVS instrument was designed and built by University of Colorado Laboratory for Atmospheric and Space Physics. The principal investigator is Nick Schneider and the Hardware lead is Bill McClintock. The EUVM instrument was also built by University of Colorado Laboratory for Atmospheric and Space Physics. The principal investigator is Frank Eparvier. The author thanks Brian J. Harding for useful discussions on the data analysis. This work was supported by the National Natural Science Foundation of China (NSFC 8206100245).

ORCID iDs

Jianqi Qin https://orcid.org/0000-0003-2213-9305

References

Bougher, S. W., Cravens, T. E., Grebowsky, J., & Luhmann, J. 2015a, SSRv, 195, 423
Bougher, S. W., Pawlowski, D., Bell, J. M., et al. 2015b, JGRE, 120, 311
Bougher, S. W., Roeten, K. J., Olsen, K., et al. 2017, JGRA, 122, 1296
Chamberlain, J. W. 1963, P&SS, 11, 901
Chaufray, J. Y., Deighan, J., Chaffin, M. S., et al. 2015, GeoRL, 42, 9031
Chaufray, J. Y., Leblanc, F., Quemerais, E., & Bertaux, J. L. 2009, JGRE, 114, E02006
Deighan, J., Chaffin, M. S., Chaufray, J.-Y., et al. 2015, GeoRL, 42, 9009
Eparvier, F. G., Chamberlin, P. C., Woods, T. N., & Thiemann, E. M. B. 2015, SSRv, 195, 293
Evans, J. S., Stevens, M. H., Lumpe, J. D., et al. 2015, GeoRL, 42, 9040
Gladstone, G. R. 1982, JQSRT, 27, 545
Gladstone, G. R. 1992, JGR, 97, 19519
Hanson, W. B., Sanatani, S., & Zuccaro, D. R. 1977, JGR, 82, 4351
Hummer, D. G. 1962, MNRAS, 125, 21
Hunten, D. M. 1973, JAtS, 30, 1481
Jain, S. K., Stewart, A. I. F., Schneider, N. M., et al. 2015, GeoRL, 42, 9023
Jakosky, B. M., Grebowsky, J. M., Luhmann, J. G., & Brain, D. A. 2015a, GeoRL, 42, 8791
Jakosky, B. M., Lin, R. P., Grebowsky, J. M., et al. 2015b, SSRv, 195, 3
Krasnopolsky, V. A. 2002, JGRE, 107, 5128
Leblanc, F., Chaufray, J. Y., Modolo, R., et al. 2017, JGRE, 122, 2401
Mahaffy, P. R., Benna, M., Elrod, M., et al. 2015, GeoRL, 42, 8951
McClintock, W. E., Schneider, N. M., Holsclaw, G. M., et al. 2015, SSRv, 195, 75
Medvedev, A. S., Nakagawa, H., Mockel, C., et al. 2016, GeoRL, 43, 3095
Meier, R. R. . 1981, ApJ, 250, 376
Meier, R. R. 1982, P&SS, 30, 439
Meier, R. R. 1991, SSRv, 58, 1
Meier, R. R., & Lee, J. S. 1978, ApJ, 219, 262
Nier, A. O., & McElroy, M. B. 1977, JGR, 82, 4341
Qin, J., & Harding, B. J. 2020, JGR, 125, e2019JA027520
Qin, J., Makela, J. J., Kamalabadi, F., & Meier, R. R. 2015, JGRA, 120, 10116
Ritter, B., Gérard, J.-C., Gkouvelis, L., et al. 2019, JGR, 124, 4809
Starr, W. L. 1976, JGR, 81, 3363
Stewart, A. I. F., Alexander, M. J., Meier, R. R., et al. 1992, JGR, 97, 91
Stone, S. W., Yelle, R. V., Benna, M., Elrod, M. K., & Mahaffy, P. R. 2018, JGR, 123, 2842
Strickland, D. J., Stewart, A. I., Barth, C. A., Hord, C. W., & Lane, A. L. 1973, JGR, 78, 4547
Strickland, D. J., Thomas, G. E., & Sparks, P. R. 1972, JGR, 77, 4052